Measurement of low-derivative surface lenses by two-laser holography with $Bi_{12}TiO_{20}$ crystals

Eduardo A. Barbosa,* Camila B. F. de Sousa, and Wellington M. Maffei

Laboratório de Óptica Aplicada, Faculdade de Tecnologia de São Paulo, Centro Estadual de Educação Technológica Paula Souza/Universidade Estadual Paulista (CEETEPS/UNESP), Pça Cel Fernando Prestes, 30 CEP 01124 060, São Paulo—SP, Brazil

*Corresponding author: ebarbosa@fatecsp.br

Received 4 June 2009; accepted 7 August 2009;
posted 20 August 2009 (Doc. ID 112338); published 10 September 2009

Refractive and profilometric analyses of lenses with large radii of curvature and/or large focal distance were performed through photorefractive holography using a $Bi_{12}TiO_{20}$ crystal as the recording medium and two red diode lasers as light sources. Both lasers were properly aligned and tuned in order to provide submillimetric synthetic wavelengths providing real-time interferograms in a two-color holography experiment. The resulting contour interferogram describes the form of the wavefront after the beam traveled back and forth through the lens. The fringe quantitative evaluation was carried out through the four-stepping technique, and the resulting phase map and the branch-cut method were employed for phase unwrapping. Exact ray tracing calculation was performed in order to establish a relation between the output wavefront geometry and the lens parameters such as radii of curvature, thickness, and refractive index. By quantitatively comparing the theoretically calculated wavefront geometry with the experimental results, errors below 1% for both refractive index and focal length were obtained.

OCIS codes: 090.2880, 210.4800, 120.5050, 210.4810, 120.4630.

1. Introduction

Most of the techniques for lens characterization, whether through purely geometric optics or through wave optics phenomena, are limited to focal length measurement only [1–4]. Nevertheless, many reverse engineering processes require the complete geometric and refractometric characterization of the lens. Adopting this approach, Anand and Chhaniwal applied digital holography for focal length, radius of curvature, and refractive index measurements [5], and Quan *et al.* measured the topography and the refractive index of a microlens array by using a sodium lamp at 589.6 nm and a He–Ne laser at 632.8 nm [6] . More recently Barbosa and Santos performed the characterization of various types of lenses by determining all their refractive and geometric parameters through multiwavelength digital speckle pattern interferometry [7]. In that work interference contour fringes were generated by employing a single diode laser emitting simultaneously many longitudinal modes centered at 660 nm as the light source. In such a configuration the contour interval (i.e., the depth difference between adjacent fringes) equals the laser resonator length, and the contour interferograms can be easily obtained in single exposure processes [8,9]. However, a limitation of this method lies in the fact that the length of the diode laser cannot be varied; hence, if the lenses to be analyzed have low-derivative surfaces the resulting contour interval—typically of the order of few millimeters—generates hardly discernible interference fringes, leading to noisy and inaccurate measurements.

In order to overcome this drawback in the present work a holographic setup with two diode lasers simultaneously emitting slightly different wavelengths, λ_1 and λ_2, was employed. By properly tuning both lasers the resulting synthetic wavelength $\lambda_S = \lambda_1\lambda_2/(\lambda_1 - \lambda_2)$ provided contour intervals $\Delta z =$

0003-6935/09/275114-07$15.00/0

$\lambda_S/2$ (i.e., the depth difference between adjacent bright fringes) that are suitable to perform the characterization of low-derivative surface lenses or small diameter lenses. The measurement of the lens curvatures and their refractive index is carried out through holographic recording with a $Bi_{12}TiO_{20}$ (BTO) crystal as the holographic medium, due to the fact that the typically high optical quality and high resolution of this crystal provides good-quality and low-noise interferograms, allowing very small contour intervals, which in turn is very desirable for the measurements of the present study. The holographic image of the studied object appears covered by interference fringes that correspond to the geometry of the reconstructed wavefront in real-time processes. As the difference $\lambda_1 - \lambda_2$ increases the interferogram spatial frequency also increases, thus enhancing the measurement sensitivity for the reconstruction of low-derivative wavefronts. It was demonstrated that whole-field, multiwavelength interferometry can be employed to surface contouring [10] or to determine the refractive index of an amorphous transparent sample [11]. The present lens characterization method combines both those profilometry and refractometry techniques in order to provide a complete description of the curvatures and the refractive index of the lens. For this purpose the wavefront shape scattered by each one of the lens surfaces and the shape of the output wave after it travels back and forth through the lens are measured. The only parameter determined by nonoptical means is the lens thickness, measured by a dial caliper. The interferograms were evaluated through the four-stepping technique for phase mappping [12] and the branch-cut method for phase unwrapping [13].

The calculation of the optical path inside the lens determines the wavefront shape as a function of the radii of curvature, the lens thickness, and the lens refractive index. This last parameter was determined by adjusting the theoretical results to the experimental data. In this work a spherical positive biconvex lens and a plano–convex doublet were analyzed.

2. Theory

Based on previous works [7,10], a brief overview of the two-laser holographic profilometry in sillenite crystals and the exact optical path calculation through refractive lenses is made in order to provide a better comprehension of the involved phenomena.

A. Two-Diode Laser Holographic Interferometry

Let us consider the interference of the reference R_N and the signal beam S_N on a BTO crystal. In the optical setup the light source is formed by two properly aligned multimode diode lasers, 1 and 2, emitting simultaneously N longitudinal modes with the same free spectral range $\Delta\nu = c\Delta\lambda/\lambda^2$, where $\Delta\lambda$ is the wavelength gap between adjacent modes and c is the light velocity. Both lasers are slightly detuned with respect to each other and emit at wavelegths λ_1 and λ_2. The waves R_N and S_N can be written at the crystal input as

$$R_N = R_0(e^{ik_1\Gamma_R} + e^{ik_2\Gamma_R}) \sum_{m=-\frac{N-1}{2}}^{m=\frac{N-1}{2}} A_m e^{i(m\Delta k\Gamma_R+\phi_m)},$$

$$S_N = S_0(e^{ik_1\Gamma_S} + e^{ik_2\Gamma_S}) \sum_{m=-\frac{N-1}{2}}^{m=\frac{N-1}{2}} A_m e^{i(m\Delta k\Gamma_S+\phi_m)}, \quad (1)$$

where $k_1 \equiv 2\pi/\lambda_1$; $k_2 \equiv 2\pi/\lambda_2$; R_0 and S_0 are the reference wave and the object wave amplitude, respectively; Γ_S and Γ_R are the optical paths of the object beam and the reference beam, respectively; $\Delta k = 2\pi\Delta\lambda/\lambda^2$; A_m is a real coefficient related to the mth mode intensity; and ϕ_m is the phase of the mth mode at the laser output.

In the readout by self-diffraction, the readout beam is the reference beam with intensity $I_R \propto {R_N}^2$. It has been shown [10] that the intensity of the holographic reconstruction can be written as a function of the diffraction efficiency η according to

$$I_S = \eta_0(1 + \chi^2 + 2|\chi|\cos 2\varphi)\left[\frac{\sin(N\gamma)}{\sin(\gamma)}\right]^2 I_R, \quad (2)$$

where $\varphi \equiv \pi(\Gamma_S - \Gamma_R)/\lambda_S, \gamma \equiv \Delta k(\Gamma_S - \Gamma_R)/2, \eta_0$ is the unmodulated diffraction efficiency, and λ_S is the synthetic wavelength defined in Section 1. The high-spatial frequency sinusoidal fringes in Eq. (2) are generated by the lasers detune $\lambda_1 - \lambda_2$ and are modulated by the low-spatial frequency envelope $[\sin(N\gamma)/\sin\gamma]^2$, which in turn is due to the multiwavelength emission of each diode laser. This undesired modulation can be eliminated either by tuning both lasers in order to operate in single frequency mode or by computational means [10]. The term $\chi < 1$ is a measure of how far from the perfect Bragg regime the holographic reconstruction occurs and decreases as $\lambda_1 - \lambda_2$ increases for $\lambda_1 \approx \lambda_2$.

The contour phase mapping is accomplished through the four-stepping method by sequentially acquiring four $\pi/2$-phase shifted interferograms with respect to the synthetic wavelength λ_S [12]. In this case the resulting phase at a point (p, q) in the wavefront can be written as

$$\phi_{4-\text{step}}(p,q) = \arctan\left(\frac{I_3(p,q) - I_1(p,q)}{I_0(p,q) - I_2(p,q)}\right), \quad (3)$$

where I_i is the intensity of the ith interferogram. The wavefront shape is then determined by unwrapping the phase map through the branch-cut technique.

B. Wavefront Shape Calculation

Figure 1 shows the optical path of the illuminating beam traveling from plane 1 to plane 2 and back to plane 1 through the spherical lens with refractive index n, thickness t, and radii of curvature R_F and R_R. The functions that describe the y coordinates

of the front and the rear surfaces in the xy plane are given by $y_F = R_F - (R_F^2 - x^2)^{1/2}$ and $y_R = t - R_R + (R_R^2 - x^2)^{1/2}$, respectively. In the experiments a flat diffusely scattering plate coinciding with plane 2 and perpendicular to the optical axis y was positioned behind the rear face of the test lens. Since the entrance pupil of the imaging lens is much smaller than the distance between the imaging lens and the test lens, the total optical path Γ corresponds to twice the path Γ_{1-2} introduced when the wave describes the path from plane 1 to plane 2 only.

Let us consider the incident beam parallel to the y direction and impinging the front surface of the lens at point A of coordinates (x_A, y_A). From Fig. 1, one sees that the total optical path of the light wave is written as a function of the segments OA, AB, and BC according to

$$\Gamma_{1\to 2} = (OA + nAB + BC), \tag{4}$$

where $OA = y_A = R_F - (R_F^2 - x_A^2)^{1/2}$.

In order to calculate the segments AB and BC, the incidence angle θ onto the lens front surface is calculated as

$$\theta = \arctan\left[-\left(\frac{\partial y_F}{\partial x}\right)^{-1}_{x=x_A}\right] = \arctan\left[\frac{x_A}{(R_F^2 - x_A^2)^{1/2}}\right], \tag{5}$$

while the beam propagation angle inside the lens (see Fig. 1) with respect to the x axis is given by $\gamma = \theta - \theta' + \pi/2$, where θ' is obtained from Snell's law:

$$\theta' = \arcsin\left\{n^{-1}\sin\left[\arctan\left(\frac{x_A}{(R_F^2 - x_A^2)^{1/2}}\right)\right]\right\}. \tag{6}$$

The beam coordinate $y_h(x)$ inside the lens is thus given by

$$y_h(x) = x\,\tan\gamma - x_A\,\tan\gamma + y_A. \tag{7}$$

The beam intersects with the lens rear surface at point (x_B, y_B), whose coordinates are given by

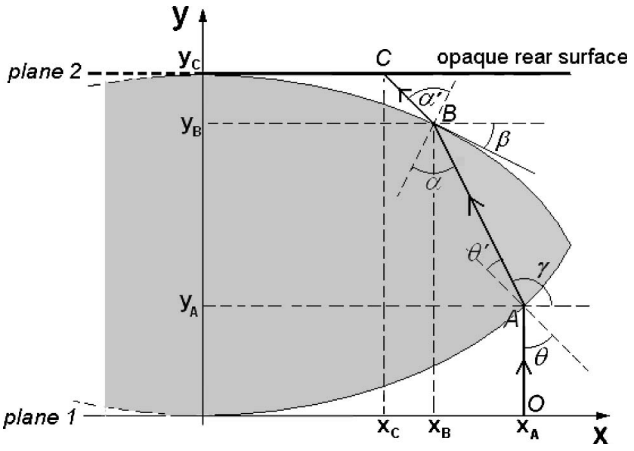

Fig. 1. Beam path into the spherical test lens.

$$x_B = -\frac{b}{2a} - \left[\left(\frac{b}{2a}\right)^2 - \frac{c}{a}\right]^{1/2},$$
$$y_B = -(x_B - x_A)\tan(\theta - \theta') + y_A, \tag{8}$$

where

$$a \equiv 1/\tan^2(\theta - \theta') + 1,$$
$$b \equiv -2/\tan(\theta - \theta')[x_A/\tan(\theta - \theta') + y_A - t + R_R],$$
$$c \equiv [x_A/\tan(\theta - \theta') + y_A - t + R_R]^2 - R_R^2. \tag{9}$$

The segment AB is written as a function of the results obtained in Eq. (8) as

$$AB = [(x_B - x_A)^2 + (y_B - y_A)^2]^{1/2}. \tag{10}$$

By proceeding analogously at the lens rear surface one obtains the angle α of the beam with respect to the normal direction at point (x_B, y_B) as (see Fig. 1)

$$\alpha = \theta - \theta' + \beta, \tag{11}$$

where

$$\beta = \left|\arctan\left[-\frac{x_B}{(R_F^2 - x_B^2)^{1/2}}\right]\right|.$$

The beam finally impinges the flat opaque plate at plane 2 at point (x_C, y_C) given by

$$x_C = x_B + (y_B - t)\tan(\alpha' - \beta), \quad y_C = t, \tag{12}$$

where $\alpha' = \arcsin[n(\sin\alpha)]$so that length BC is thus given by

$$BC = [(x_C - x_B)^2 + (y_C - y_B)^2]^{1/2}. \tag{13}$$

From Eqs. (4) and (13) the total optical path of the beam in the xy plane is thus given by

$$\Gamma_{1\to 2} = y_A + n[(x_B - x_A)^2 + (y_B - y_A)^2]^{1/2} + [(x_C - x_B)^2 + (y_C - y_B)^2]^{1/2}. \tag{14}$$

This calculation can be carried out similarly for other lens types, such as toric and parabolic lenses. For toric (or spherocylindrical) lenses the coordinates y_F and y_R are calculated for both the xy and the yz planes in order to take into account the different focal lengths in each plane, while for parabolic lenses y_F and y_R describe parabolic curves. Hence, from the relation

$$\theta = \arctan\left[-\left(\frac{\partial y_F}{\partial q}\right)^{-1}_{x=x_0}\right]$$

(where $q = x$ or z), the rest of the calculation is performed straightforwardly.

In Section 3 the reconstructed wavefront profiles obtained from the experimental results are quantitatively compared with the optical path calculated in Eq. (14), thus providing the refractive index of the studied lens.

3. Experiments and Results

Figure 2 shows the holographic setup with two 30 mW diode lasers with emission centered at 670 nm. Both lasers were coupled by the beam splitter BS with the help of mirror M4. The object was imaged at the BTO by lens L2, while lens L3 formed the holographic image at the target of the CCD camera. The holographic image was displayed at the computer monitor for further processing and analysis and the holographic recording time was ~10 s. The beam illuminating the object has a plane wavefront due to the afocal telescope L1, and the intersection region of the reference and the object beams inside the crystal was adjusted to be ~2 mm, due to the Bragg selectivity of the holographic recording in a thick grating [10]. In order to enhance the signal-to-noise ratio of the holographic image by exploring the anisotropic diffraction properties of the sillenite crystals the transmitted object beam was blocked by polarizer P2 [14]. The superposition of the interfering beams at the BTO input during the phase stepping was ensured by a 90° prism, PR, mounted on the translation stage. The other BTO output containing the transmitted reference beam and its holographic reconstruction was delivered to a spectrometry goniometer with a 600 line/mm diffraction grating for spectrum measurement. This device was used with the purpose of giving initial information about the laser spectra only, since its low resolution was not suitable to provide the synthetic wavelength with accuracy. The lasers were tuned by properly selecting their driving currents.

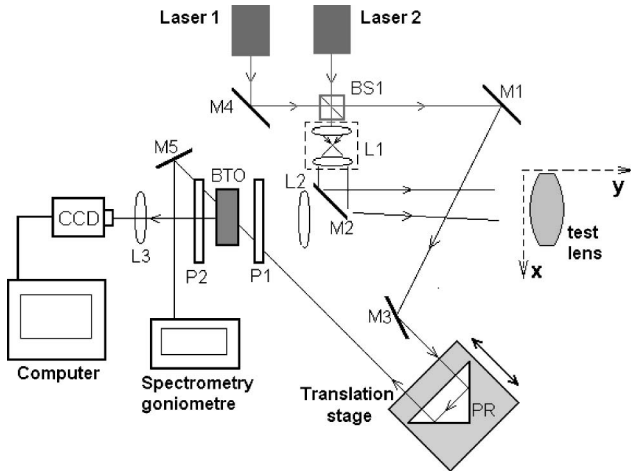

Fig. 2. Optical setup: M1–M5, mirrors; L1– L3, lenses; P1 and P2, polarizers; BS1, beam splitter; PR, 90° prism; BTO, $Bi_{12}TiO_{20}$ crystal; CCD, camera.

A. Biconvex Lens

In order to compare the performance of the optical setup with one laser and with two lasers, the holographic imaging was first carried out with multimode laser 1 only. Figure 3(a) shows the holographic image of the front surface of the nearly symmetric biconvex 5.9 mm thick spherical lens made of BK7 glass, showing that the typically large contour interval of 3.30 mm generated by only one laser cannot provide discernible contour fringes due to the low-derivative character of the lens surface. The surface was covered by a 25 μm thick PVC film by hand in order to make it opaque. The irregularities in the film thickness are much smaller than the radii of curvature uncertainties and therefore can be considered negligible to the measurements. Both diode lasers were then used and tuned in order to provide the values $\lambda_1 = 670.2$ nm and $\lambda_2 = 670.9$ nm, resulting in the contour interval $\Delta z = 0.32$ mm for measuring the lens shape through the four-stepping method and the unwrapping process. The high-spatial frequency contour interferogram of the front surface obtained with both lasers is shown in Fig. 3(b), Fig. 3(c) shows the corresponding phase map obtained through the four-stepping technique, and Fig. 3(d) shows the reconstructed wavefront after phase unwrapping. Figure 3(e) shows the averaged y coordinate (thick black curve) of the lens surface taken along radial directions such as line AB shown in Fig. 3(d). The radius of curvature of each surface was determined through such curve by fitting the experimental data with the function $R - (R^2 - x^2)^{1/2}$ [thin gray curve of Fig. 3(e)]. The analysis provided radii of curvature $R_F = 33.2$ mm and $R_R = 32.9$ mm.

For refractive index measurement, the films were removed and the flat opaque surface was positioned behind the lens, so that the illuminating beam crossed the lens and impinged the plate as described in Subsection 2.B and depicted in Fig. 1. The resulting contour fringe pattern of one of the four frames for $\Delta z = 0.24$ mm is shown in Fig. 4(a), while Fig. 4(b) shows the averaged y coordinate of the reconstructed wavefront obtained similarly as in Fig. 3(d). The thick black line refers to the measured coordinates, while the thin gray one is the fitting of the experimental data with the Γ values given by Eq. (14). The best computational fitting in this case was obtained for $n = 1.50 \pm 0.01$ through the chi-square method. The measurement error defined as $\delta(\%) = 100|n - n_E|/n_E$ was estimated to be ~0.7%, considering the expected value for red light of $n_E = 1.514$.

The nominal focal length of the lens provided by the manufacturer is 32.4 mm, while the experimental value for $R_F = 33.2$ mm, $R_R = 32.9$ mm, $t = 5.95$ mm, and $n = 1.50$ was calculated to be 32.1 mm, which corresponds to an experimental error of ~0.9%. The focal length was calculated from the well-known formula

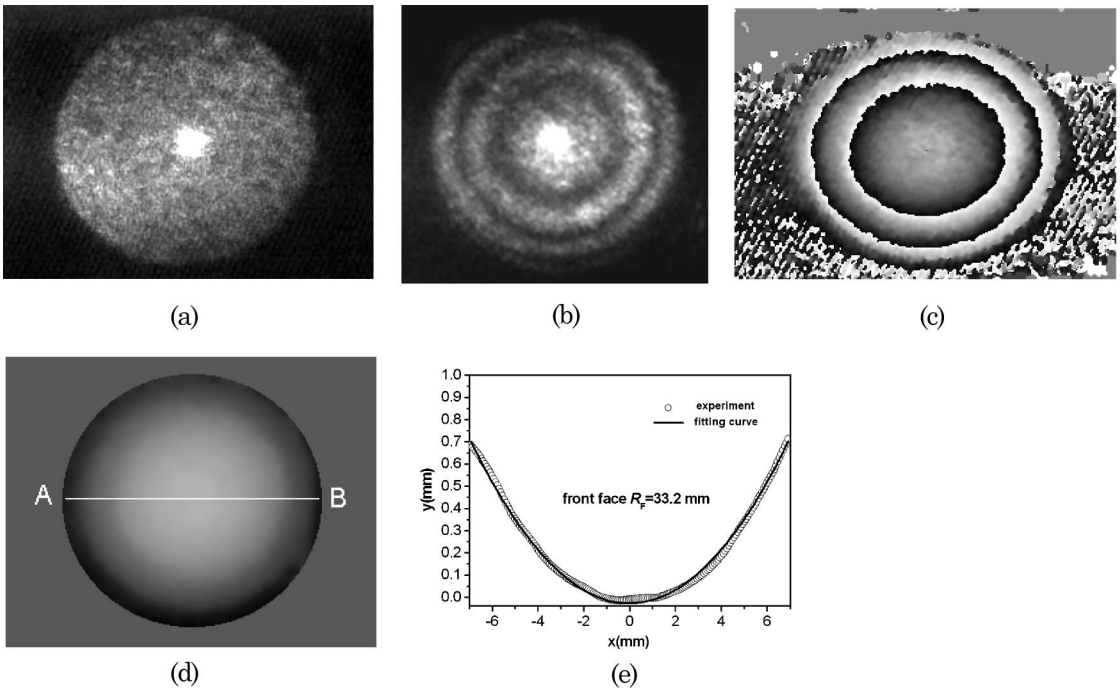

Fig. 3. (a) Holographic image of the biconvex lens generated by only one laser ($\Delta z = 3.3$ mm). (b) Two-diode laser holographic image of the same surface for $\Delta z = 0.32$ mm. (c) Phase map obtained through the four-stepping technique. (d) Reconstructed wavefront after phase unwrapping. (e) y coordinate (thick black curve) averaged along radial directions and a fitting curve (thin gray curve) providing $R_F = 33.2$ mm.

$$\frac{1}{f} = (n-1)\left[\frac{1}{R_F} - \frac{1}{R_R} + \frac{t}{R_F R_R}\frac{(n-1)}{n}\right]. \quad (15)$$

B. Plano–Convex Achromatic Doublet

Our technique can also be employed for determining the focal length of achromatic doublets. In this case we considered an equivalent refractive index, since such lenses are made of a negative and a positive lens with different refractive indices and different Abbe numbers. We studied a plano–convex cemented-Fraunhofer type lens illuminated as shown in Fig. 5; in this case, the focal length can be obtained from the paraxial ABCD matrix formalism [15] as

$$\frac{1}{f} = \frac{n_a - n_b}{R_D} + \left(\frac{n_a - 1}{R_D}\right)\left[1 - \left(\frac{n_a - n_b}{n_a}\right)\frac{t_a}{R_D}\right], \quad (16)$$

where R_D is the radius of curvature of the symmetrical biconvex lens with refractive index n_a and thickness t_a, while n_b is the refractive index of the plano–concave lens. Since our two-laser holographic technique does not distinguish the refractive indices of both lenses, it is convenient to introduce the equivalent refractive index n_{eq}, through which the focal length of the plano–convex lens is given as

$$\frac{1}{f} = \frac{n_{eq} - 1}{R_D}, \quad (17)$$

as if the achromatic doublet were an ordinary single plano–convex lens with refractive index n_{eq}, whose scheme is shown in the inset at the top of Fig. 5. By combining Eqs. (16) and (17) n_{eq} can be given by

$$n_{eq} = 2n_a - n_b - \frac{(n_a - n_b)(n_a - 1)}{n_a}\frac{t_a}{R_D}. \quad (18)$$

Equation (18) shows that it is meaningful to consider the existence of an equivalent refractive index that depends not only on the refractive indices of the doublet components but also on their geometry.

In order to obtain the relief of the lens the same procedure as in Subsection 3.A was performed. Figure 6 shows the averaged profile (thick black curve) of the lens spherical surface obtained from its holographic 3-D reconstruction and the respective fitting to a circle function (thick gray curve), showing a radius of curvature of $R_D = 21.53$ mm. The optical path of the reconstructed wavefront after the light propagates through the uncovered lens back and forth is shown in Fig. 7, providing the equivalent refractive index of $n_{eq} = 1.64 \pm 0.01$. From Eq. (17) the focal distance of the lens was calculated to be 33.4 mm, versus the figure of 32 mm provided by the lens manufacturer, resulting in an error of 4.4%.

The discrepancies between the experimental values and the expected ones can be attributed mainly to three sources: fluctuation of the lasers wavelengths, errors in determining the contour interval, and the noncollimated beam illuminating the object. The first error source is due to the transient thermal behavior of the lasers and/or to mode hopping, i.e., competition between laser modes, leading to small

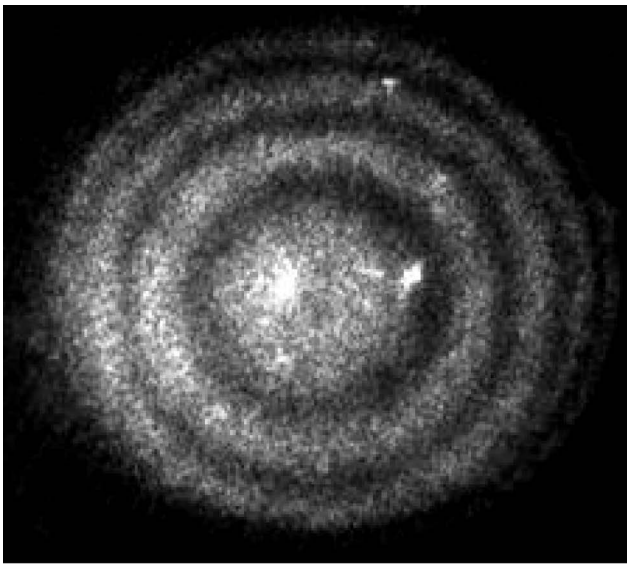

(a)

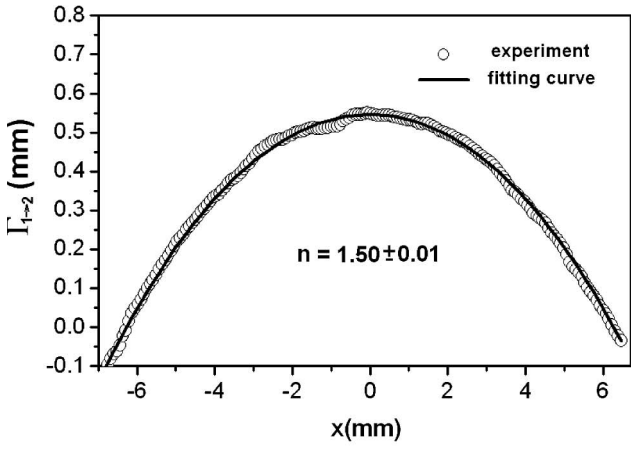

(b)

Fig. 4. (a) Contour fringe pattern for $\Delta z = 0.24$ mm when the illuminating beam traveled through the lens. (b) Averaged y coordinate of the reconstructed wavefront providing $n = 1.50 \pm 0.01$.

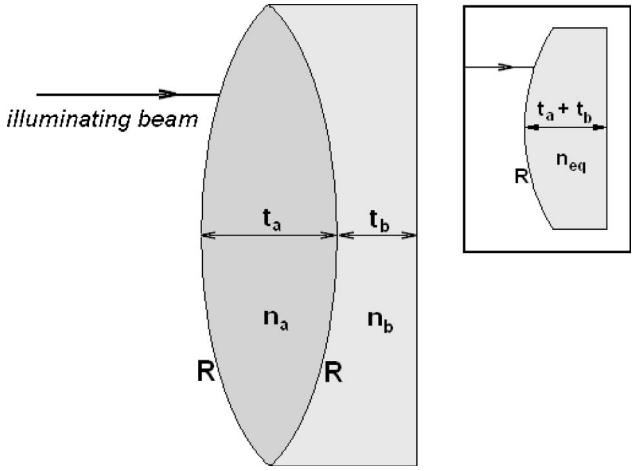

Fig. 5. Plano–convex achromatic doublet.

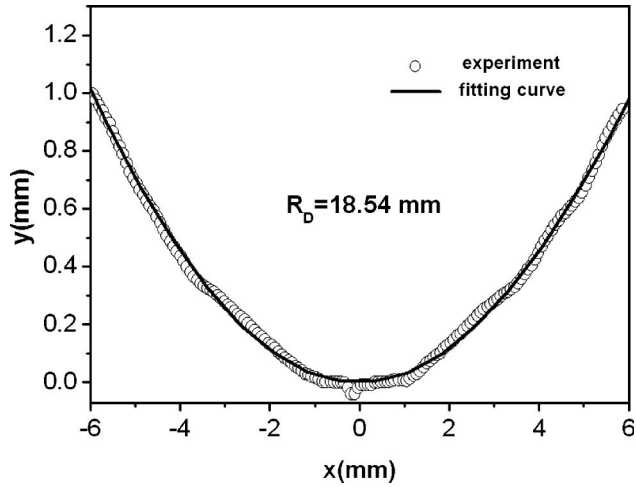

Fig. 6. Averaged profile of the doublet spherical surface (thick black curve) and fitting curve providing $R_D = 21.53$ mm (thin gray curve).

but eventually important variations in the synthetic wavelength. This problem can be minimized by supplying the lasers with highly stabilized voltages and by using temperature controlled diode lasers, which were not available at our laboratory. The contour interval in turn was determined experimentally by translating the micrometric screw and measuring the displacement for which an integer number of fringes were displaced. The small number of fringes and the visual character of the measurement may lead to errors. Such errors can be avoided by sending the transmitted reference beam to a narrowband high-resolution CCD-based spectrometer through which λ_1 and λ_2 can be measured in real time and λ_S can thus be determined with high precision and accuracy. The third error source is the least probable one in our experiments, since calibration measurements were performed before the lens measurements by using a flat surface as the object in order to estimate the radius of curvature of the illuminating beam.

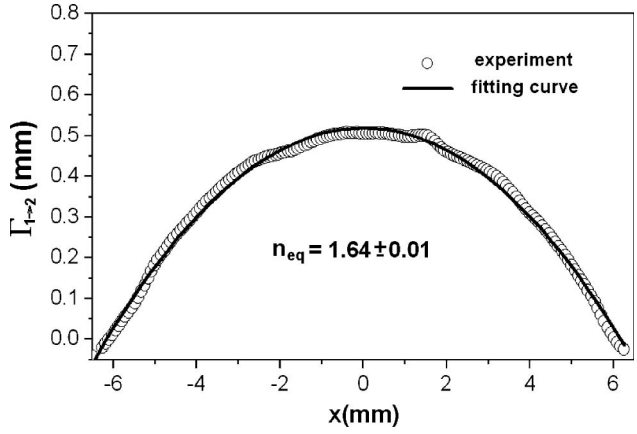

Fig. 7. Optical path of the reconstructed wavefront after the light propagates through the uncovered lens providing $n_{eq} = 1.64 \pm 0.01$.

4. Conclusion

In this work the curvature and the refractive index of a biconvex lens and a plano–convex doublet were measured by two-diode laser photorefractive holography. Unlike most lens characterization methods, the method presented in this article does determine all the relevant physical parameters of the lens, thus providing a complete description of the refraction suffered by the illuminating wave. Through exact ray tracing the possible geometric aberrations of the lens are automatically taken into account, leading to more precise and accurate measurements, if compared to approximative methods such as paraxial ray tracing. The use of an optical arrangement with two spatially coupled diode laser beams provides good flexibility in selecting the synthetic wavelength, thus enabling more accurate and less noisy measurements. Moreover, the employment of detuned lasers simultaneously allowed us to obtain real-time interferograms. In spite of the measurement discrepancies, the experiments in general can be considered fairly satisfactory. The most relevant error sources as well as the possibilities of minimizing them were pointed out, showing the promising potentialities of the technique.

The BTO crystal provided good-quality holographic images in relatively fast measurements. The visibility of the interference fringes was mainly limited by the Bragg condition related to the volume grating thickness. This limitation cannot be significantly overcome by using, e.g., thinner BTO samples, since in this case the hologram diffraction efficiency as well as the signal-to-noise ratio would decrease remarkably.

We acknowledge fruitful discussions with L. P. G. Dib from Faculdade de Tecnologia de São Paulo. This work was partially sponsored by Conselho Nacional de Desenvolvimento Científico e Tecnológico (CNPq) under grant 473458/2006-3. C. B. F. de Souza received a scholarship from CNPq, and W. M. Maffei received a scholarship from Fundação de Amparo à Pesquisa do Estado de São Paulo (Fapesp).

References

1. M. de Angelis, S. de Nicola, P. Ferraro, A. Finizio, G. Pierattini, and T. Hessler, "Interferometric method for measuring short focal length refractive lenses and diffractive lenses," Opt. Commun. **160**, 5–9 (1999).
2. C. J. Tay, M. Thakur, L. Chen, and C. Shakher, "Measurement of focal length of lens using phase shifting Lau phase interferometry," Opt. Commun. **248**, 339–345 (2005).
3. E. Keren, K. M. Kreske, and O. Kafri, "Universal method for determining the focal length of optical systems by moire deflectometry," Appl. Opt. **27**, 1383–1385 (1988).
4. R. A. Arizaga, J. A. Pomarico, and R. D. Torroba, "Digital technique for high accuracy focal length measurements," Opt. Commun. **152**, 6–10 (1998).
5. A. Anand and V. Chhaniwal, "Measurement of parameters of simple lenses using digital holographic interferometry and a synthetic reference wave," Appl. Opt. **46**, 2022–2026 (2007).
6. C. Quan, S. H. Wang, C. J. Tay, I. Reading, and Z. P. Fang, "Integrated optical inspection on surface geometry and refractive index distribution of a microlens array," Opt. Commun. **225**, 223–231 (2003).
7. E. A. Barbosa and S. C. dos Santos, "Refractive and geometric lens characterization through multiwavelength digital speckle pattern interferometry, "Opt. Commun. **281**, 1022–1029 (2008).
8. E. A. Barbosa, "Holographic imaging with multimode, large free spectral range lasers in photorefractive sillenite crystals," Appl. Phys. B **80**, 345–350 (2005).
9. E. A. Barbosa, A. A. V. Filho, M. R. R. Gesualdi, B. G. Curcio, M. Muramatsu, and D. Soga, "Single-exposure, photorefractive holographic surface contouring with multiwavelength diode lasers," J. Opt. Soc. Am. A **22**, 2872–2879 (2005).
10. E. A. Barbosa and J. F. Carvalho, "Surface analysis by two-diode laser photorefractive holography," Appl. Phys. B **87**, 417–423 (2007).
11. E. A. Barbosa, R. Verzini, and J. F. Carvalho, "Multi-wavelength holography in $Bi_{12}TiO_{20}$ crystals: applications in refractometry," Opt. Commun. **263**, 189–196 (2006).
12. K. Creath, "Phase-measurement interferometry techniques," Prog. Opt. **26**, 349–393 (1988).
13. B. Gutmann and H. Weber, "Phase unwrapping with the branch-cut method: clustering of discontinuity sources and reverse simulated annealing," Appl. Opt. **38**, 5577–5593 (1999).
14. A. A. Kamshilin and M. P. Petrov, "Continuous reconstruction of holographic interferograms through anisotropic diffraction in photorefractive crystals," Opt. Commun. **53**, 23–26 (1985).
15. E. Hecht, *Optics* (Addison-Wesley, 1998).